200 MeV Proton Radiography Studies with a Hand Phantom Using a Prototype Proton CT Scanner

Tia Plautz, V. Bashkirov, V. Feng, F. Hurley, R.P. Johnson, C. Leary, S. Macafee, A. Plumb, H.F.W. Sadrozinski, K. Schubert, R. Schulte, B. Schultze, D. Steinberg, M. Witt, A. Zatserklyaniy

***Abstract*—Proton radiography generates two-dimensional projection images of an object and has applications in patient alignment and verification procedures for proton beam radiation therapy. The quality of the image, both contrast and spatial resolution, is affected by the energy of the protons used in the creation of the radiograph, as well as by multiple Coulomb scattering and energy-loss straggling. Here we report an experiment which used 200 MeV protons to generate proton energy-loss and scattering radiographs of a hand phantom. It was found that while both radiographs displayed anatomical details of the hand phantom, the energy-loss radiograph has a noticeably higher spatial resolution. The scattering radiograph may yield sharper edges between soft and bone tissue than energy loss radiograph, but this requires further study. These radiographs demonstrate the new promise of proton imaging (proton radiography and CT) now within reach of becoming a new, potentially low-dose medical imaging modality. The experiment used the current first-generation proton CT scanner prototype, which is installed on the research beam line of the clinical proton synchrotron at Loma Linda University Medical Center. This study contributes to the optimization of the performance of a clinical proton CT scanner.**

***Index Terms*—proton imaging, tomographic reconstruction of material properties, spatial resolution, data reduction**

I. Introduction

With increasing use of proton radiation therapy for cancer patients, research into new imaging methods that can improve the accuracy of proton range estimates in radiation therapy planning have become a high priority. Protons are particularly desirable for treating cancerous tissue in close proximity to radiosensitive normal tissues, such as at the base of skull and near the spinal cord. Protons are preferable to photons because their energies are easily tuned, the unhealthy area can be isolated, and the dose can be localized reducing the threat of damaging otherwise healthy tissue. Most importantly, the greatest radiation dose occurs only in the last 2% of the proton's range, at the Bragg peak, so a maximum amount of healthy tissue can be spared when the position of the Bragg peak is controlled.

Tia Plautz, V. Feng, R. P. Johnson, C. Leary, S. Macafee, A. Plumb, H. F. W. Sadrozinski, D. Steinberg and A. Zatserklyaniy are with the Santa Cruz Institute for Particle Physics, University of California Santa Cruz, Santa Cruz, CA 95064 USA (e-mail: tiaplautz@gmail.com).

V. Bashkirov, R. F. Hurley, R. Schulte are with Loma Linda University Medical Center, Loma Linda, CA 92354 USA.

K. Schubert, B. Schultze, M. Witt are with CSU San Bernardino, San Bernardino, CA 92407 USA.

Manuscript received 11 December, 2012.

This work was supported in part by Grant No. 1R01EB013118-01 from the National Institute of Health.

In order to obtain relative stopping power (RSP), Hounsfield units (i.e. units of x-ray attenuation used in x-ray CT) are transformed using a calibration curve. However, there is no unique relationship between Hounsfield units and RSP, especially in the regime of RSP=1 (i.e. water, human tissue). This means that during conversion, errors in proton range are consistently 3-4% of the nominal proton range or even higher in regions containing bone [1]. A recent survey by the American Association of Physicists in Medicine (AAPM) showed that 33% of attendees polled said that range uncertainties are the main obstacle to making proton therapy mainstream [2]. Simulations and first experimental results have shown that using a proton CT imaging system one may be able to reduce this range uncertainty to about 1% or less without increasing the dose to the patient.

Proton CT differs in several key aspects from x-ray CT. While unscattered photons travel in straight line paths, protons do not and rather undergo many multiple Coulomb scattering (MCS) events, which limits the usefulness of the standard filtered back projection (FBP) approach to reconstruction. In fact, proton CT images reconstructed with the classical FBP algorithm suffer from loss of spatial resolution since the proton path deviates from the assumed straight lines by up to several millimeters in anatomical objects encountered in medical proton CT imaging. The accuracy of those path estimates is critical for achieving a high spatial resolution in proton CT.

A. Current Prototype Design

A low intensity, high energy (100-200 MeV) cone beam of protons traverses a phantom. Silicon strip detectors (228 μm pitch) record the proton path in 4 planes (each 400 um thick) so entry and exit vectors can be easily determined. Detectors interface through a high speed field programmable gate array (FPGA)-based data acquisition system. A calorimeter composed of an array of 18 CsI crystals is used to detect the residual energies of incident protons at a rate of up to 100k protons/sec.

B. Reconstruction Software

Mathematical algorithms and computer software are used to reconstruct the phantom from raw data [3]. Raw data contain the proton tracker coordinates and the calorimeter's response for each proton. The software bins the exit tracker data into spatial bins (pixels) and determines cuts in relative angle, defined as the difference between entry and exit angle, at 3σ

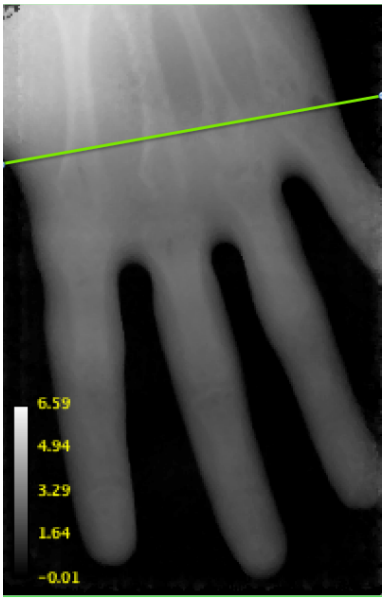

Fig. 1 – First radiograph of a hand phantom with 0.5 mm pixels (scale in cm of WEPL). The RSP of bone is only about 50% greater than that of water, resulting in the low contrast between the bones and soft tissue. The line traversing the image corresponds to the image profile analyzed in Fig. 4.

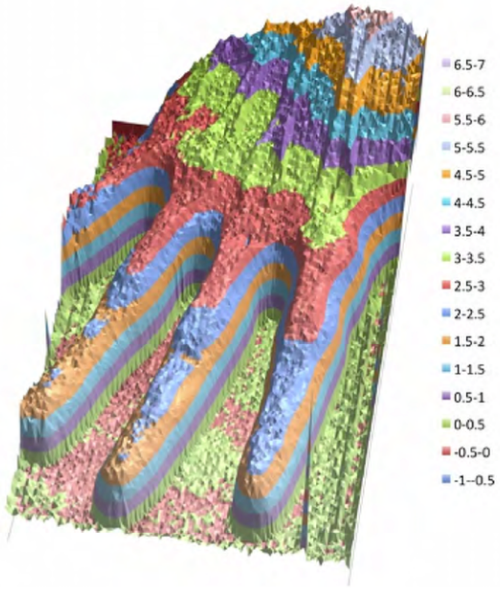

Fig. 2 – Radiograph of a hand phantom (Fig. 1) in terms of water equivalent thickness (WET) calculated from the summed-up stopping power of the phantom. The image shows the varying thickness of the hand and clear structural details. The scale on the right hand side is in cm.

from each pixel's mean relative scattering angle. These cuts are made to exclude events that have very large scattering angles, caused by inelastic nuclear interactions or elastic large angle scattering events inside the phantom. The software also makes cuts in water equivalent path length (WEPL) given by:

$$L = \int_{\ell} \varrho d\ell, \tag{1}$$

where ϱ is the ratio of the stopping power of the material to the stopping power of water (i.e. the RSP) and ℓ defines the path of the proton. These cuts are also made at 3σ from the mean pixel value, and are necessary to insure that erroneously large energy measurements, caused by the coincidence of two or more particles in the calorimeter, are excluded.

II. Energy-Loss Radiography and Water Equivalent Path Length (WEPL)

The quantity of importance for proton treatment planning is relative stopping power (RSP) of protons with respect to water. RSP, or ϱ in Eq. 1, is practically energy independent and is determined mostly by the electron density of the material or tissue.

We calibrate the calorimeter response to the integral of the RSP directly. For each pixel, we define a mode window of WEPL that accepts protons within $\pm$ 30% of the mode, or ± 1 cm if 30% is less than 1 cm, and make the appropriate cuts during reconstruction. Fig. 1 is a radiograph of a hand phantom using this energy-loss technique and data reduction process.

The WEPL distribution of protons in each pixel is roughly gaussian, as seen in Fig. 3(a). The distribution is usually skewed to the right (high WEPL) which corresponds to the left-skewed (low-energy) distributions in energy. The protons in the tails are protons that underwent nuclear scattering events. These are the events that we wish to reduce by appropriate cuts.

We did find that a significant percentage of pixels contained non-gaussian, or anomolous WEPL distributions. These distributions, as in 3(b), are bimodal and correspond to pixels that lie on the boundary between two materials of different RSP. Currently, the reconstruction algorithm selects the mode that is closest to the mean, and the appropriate cuts are determined based on that value. This, however, ignores valuable information and leads to lower spatial resolution. Methods such as averaging the two modes, or "splitting" pixels have been proposed and have yet to be explored.

An image of the radiographic hand phantom in terms of WEPL (Fig. 1 and 2) was created by plotting values of WEPL for each pixel (in cm). The image clearly depicts the varying thickness of the hand in different places, and shows clear structural details. The agreement between this image and the phantom shows that there is great promise in our technique.

As a further exploration of WEPL, we investigated radiographs of various pixel sizes: 1-mm, 0.5-mm, 0.25-mm. The plots in Fig. 4 illustrate the image profile along the line indicated in Fig. 1 for the various pixel sizes. Fig. 4 shows that as pixel size is systematically decreased, the steepness of the slope of the image profile increases from a relatively shallow incline in the 1-mm (pixel size) plot to a steep rise from 0 to 1 cm of WEPL in the 0.25-mm plot, due to the improved spatial resolution with smaller pixel size. However, decreasing the size of the pixel also increases the amount of spatial noise added to the profile, due to the lower statistics (fewer protons in each pixel). While some regions of the 0.5 mm and the 0.25 mm plots are relatively sharp, other regions are entirely washed out with almost no way to tell what the signal actually is. One can increase the number of protons, but this will increase the dose to the patient, which should be

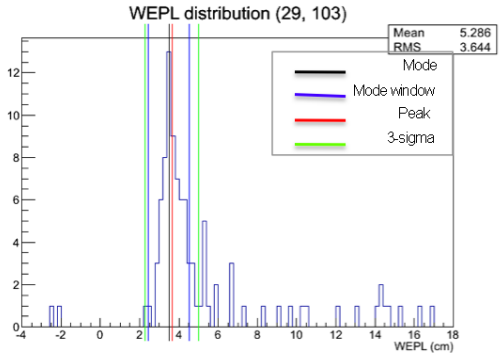

(a)

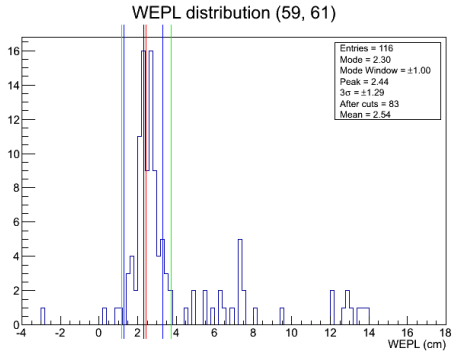

(b)

Fig. 3 – Distribution in WEPL for pixels described by the coordinates 3(a) ($v = 29, t = 103$) and 3(b) ($v = 61, t = 59$) before cuts are made. The black line defines the mode of the distribution and the red line defines the mean or "peak" of the distribution. The blue lines indicate the mode window which contains the particles within $\pm 30\%$ of the mode, and provides the distribution on which the 3σ cuts are based. The green lines indicate the cuts made on this specific pixel. Notice the straggling in the large WEPL range. These values correspond to particles that underwent nuclear interactions. Fig 3(a) illustrates an example of a roughly gaussian WEPL distribution. Fig. 3(b) is that for a boundary pixel with a bimodal WEPL distribution.

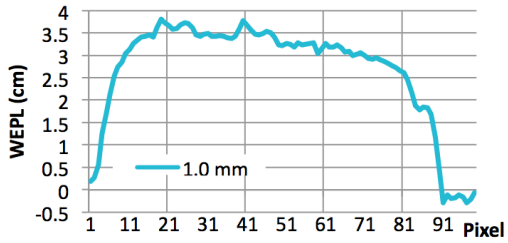

(a) 1-mm pixels

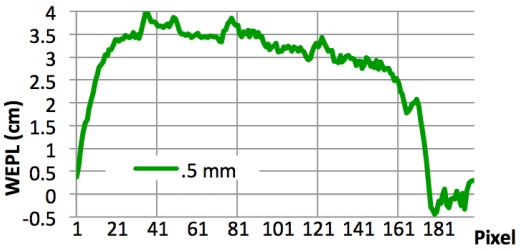

(b) 0.5-mm pixels

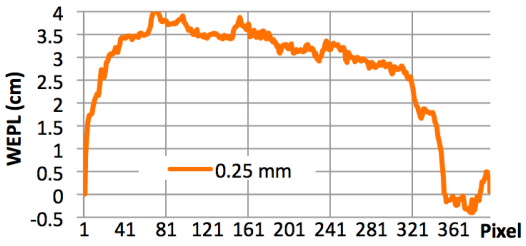

(c) 0.25-mm pixels

Fig. 4 – Image profiles for 1-mm, 0.5-mm and 0.25-mm pixels. Profiles show that as pixel size is decreased from 1-mm (Fig. 4(a)) to 0.5-mm (Fig. 4(b)), the spatial resolution increases (i.e. the details become more clear). Further reducing the pixel size seems only to increase statistical noise in the image (Fig. 4(c)). An ideal pixel size must be found that maximizes spatial resolution while minimizing dose delivered to the patient.

kept as small as possible due to the small risk of secondary cancer. This analysis suggests that, for a given dose, there is an ideal pixel size which will provide a balance between spatial resolution and dose. We have found that at least 20 protons/pixel are required for reasonable statistics.

III. Multiple Coulomb Scattering and Proton Scattering Radiography

The amount that a proton is scattered between its entry and exit from a phantom is proportional to the inverse of its energy and can be described by the Lynch-Dahl approximation for multiple scattering events [4]:

$$\theta = \frac{13.6eV}{\beta cp} z \sqrt{\frac{x}{X_o}} [1 + 0.038 \log \frac{x}{X_o}] \qquad (2)$$

where θ is the width of the Gaussian approximation for angular deflection in a plane, β, p are the velocity and momentum of the proton, respectively, z is the charge of the proton and x/X_o is the thickness of the material traversed in radiation lengths, where we calculate X_o of the material using:

$$\frac{1}{X_o} = \sum \frac{w_j}{X_j} \qquad (3)$$

where the w_j's are the fractions by weight of each element in a given material. The second term in Eq. 2 tends to be small and can thus be ignored for purposes of estimation. Note that this approximation is good only for relatively thin objects (i.e. $10^{-3} < x/X_o < 100$) where the energy and momentum are assumed to be approximately constant. For a thicker phantom, we must account for energy-loss by introducing an integral over x (see Ref. [5] for details).

A scattering radiograph (scale in mrad) is given in Fig. 5. A gaussian distribution of scattering angles in each of the t (vertical) and v (horizontal) planes in each pixel was obtained. The mean v and t angles were determined in each

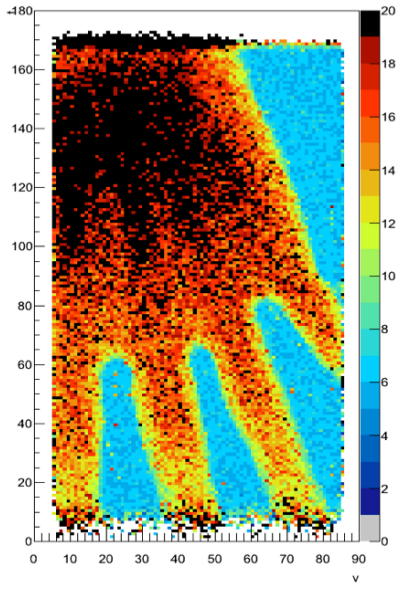

Fig. 5 – This scattering radiograph shows a strong agreement between predicted thickness given by Eq. 2 and the thickness of real materials. Variation in the thickness of the hand is clearly visible. Regions of dark orange and black are those corresponding to thick regions of bone. Blue region in the background corresponds to the scattering due to SSD's alone. Scale is in mrad.

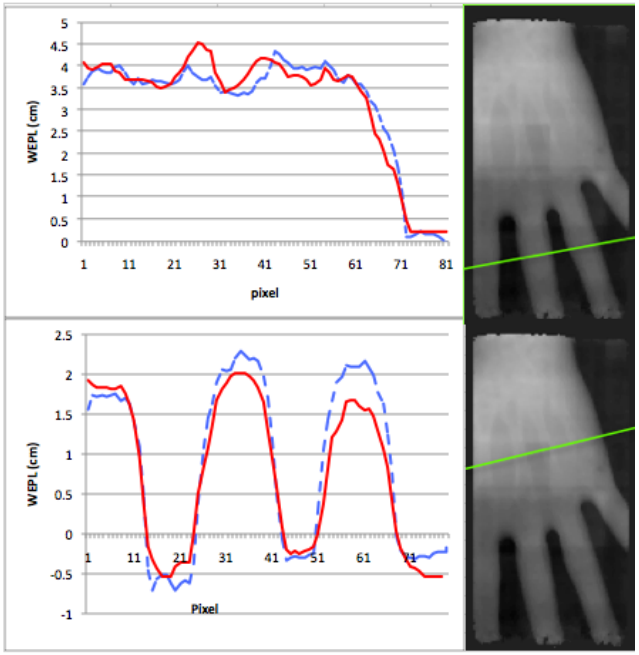

Fig. 6 – Normalizing the scattering radiograph (solid curve) to the energy-loss radiograph (dashed curve), we see roughly the same shape and even some subtle features, however these are quite a bit washed out. The profile slopes of the scattering radiograph in the bottom plots are shallower, indicating reduced spatial resolution.

pixel from these distributions. These mean angles were added in quadrature in order to obtain the mean spatial scattering angle, defined as the angle of scattering from the beam axis. Areas of high scattering power, such as bone, were expected to yield greater scattering angles, while protons scattered only by SSDs were expected to have the smallest scattering angle. The scattering angle value was then compared with the expected scattering estimated using Eq. 2.

TABLE I – Densities and radiation lengths of materials commonly encountered in pCT. Data for bone: [6]. Data for tissue, water and silicon: [7]

Material	Density (g/cm^3)	Radiation Length, X_o (g/cm^2)
bone	1.45	16.6
tissue	1.00	38.2
water	1.00	36.1
silicon	2.33	21.8

Table I provides radiation length values for material that we typically deal with in medical proton imaging. For a 200 MeV proton, $\beta = .566$ and $p = 644$ MeV/c, and therefore, by Eq. 2, the scattering due to the four silicon tracker plates (1.6 mm total thickness) is expected to be approximately 5.2 mrad. Comparing this estimate with the background (blue) region in Fig. 5, we find that this estimate agrees well with the image, which depicts scattering of 5-6 mrad due to the SSD's alone.

While the spatial resolution of the scattering radiograph is not as good as with the energy-loss radiograph, one can still observe regions of varying thickness around the edges of the fingers, where the protons traversed only skin and soft tissue (yellow and green region), and in the hand, where the thickest bone exists (black region). The scattering angles correspond to realistic proton path lengths through the hand.

A remarkable aspect of scattering radiography is that the contrast between bone and soft tissue for proton scattering power is, in principle, higher than that of proton stopping power. The stopping power of bone is 50% - 80% greater than that of water, but the scattering power of bone is about 2.5 times that of water. Fig. 6 compares two image profiles for the energy-loss radiograph (dashed curve) and the scattering radiograph (solid curve). When the scattering curve is normalized to the energy-loss curve, we find that the general shapes of the two curves of each plot are almost identical, which shows that in this case, regions of greater stopping power are also regions of higher scattering power. The energy-loss curve clearly provides higher spatial resolution, but more importantly, it provides the RSP information required for treatment planning. The scattering radiograph, however, may provide us with higher contrast resolution, since contrast depends upon the difference in material properties of those materials being imaged. Information about the radiation length of the material, X_o can be gleaned from the scattering radiograph and can provide us with the the effective atomic number of the material, Z (which is inversely proportional to the radiation length). The quality and usefulness of this information, however, requires further investigation.

IV. Conclusion

Our proton radiographs demonstrate the new promise of proton imaging (proton radiography and CT) now within reach of becoming a new, potentially low-dose medical imaging modality. This work indicates that choosing an optimal pixel size is important for balanced image quality in terms of low-contrast and spatial resolution. The image profile comparison suggests that scattering radiography may yield sharper edges

(greater contrast) between soft and bone tissue than energy loss radiography, alone. However, this requires further study. Scattering radiography (like x-ray radiography) does provide information about the radiation length of materials which is inversely proportional to the effective atomic number distribution in the tissue. Energy-loss radiography cannot provide this information since stopping power depends only on Z/A which is practically identical for most soft tissues and water, leading to very low contrast. Therefore, scattering radiography will likely have useful applications in proton treatment planning.

ACKNOWLEDGMENT

We acknowledge contributions from Y. Censor (The University of Haifa (Israel)), S. Penfold (University of Wollongong (Australia)), and R. Davidi (Stanford University).

This research in proton CT is supported by the National Institute of Biomedical Imaging and Bioengineering (NIBIB), and the National Science Foundation (NSF), award Number R01EB013118, the U.S. Department of Defense Prostate Cancer Research Program, award No. W81XWH-12-1-0122, and the United States - Israel Binational Science Foundation (BSF). The content of this poster is solely the responsibility of the authors and does not necessarily represent the official views of NIBIB, NIH, NSF and DOD.

The proton imaging detectors were built at UCSC and Northern Illinois University with support from the U.S. Department of Defense Prostate Cancer Research Program, award No. W81XWH-12-1-0122 and the Department of Radiation Medicine at LLU.

REFERENCES

[1] R. Schulte. A Status Update on Proton Imaging for Applications in Medicine. IEEE Nuclear Science Symposium and Medical Imaging Conference. Anaheim. 30 Oct. 2012.

[2] Tami Freeman. Will protons gradually replace photons? Medical Physics Web. 22 August, 2012. http://medicalphysicsweb.org/cws/article/research/50584.

[3] S. Penfold, Image Reconstruction and Monte Carlo Simulations in the Development of Proton Computed Tomography for Applications in Proton Radiation Therapy PhD thesis Univ. of Wollongong, 2010.

[4] Particle Data Group. *Review of Particle Physics 2008*. Section 27.3 "Multiple scattering through small angles." p. 271. 2008.

[5] Schulte R.W., Penfold S. N., Tafas J. T., and Schubert K. E., A maximum likelihood proton path formalism for application in proton computed tomography, Med. Phys. 35: 4849-4856, 2008.

[6] D. C. Williams, Phys. Med. Biol. 49 (2004) 2899-2911.

[7] Particle Data Group. Atomic and Nuclear Properties of Materials for more than 300 Materials. Accessed 15 November, 2012. http://hepdata.cedar.ac.uk/lbl/2011/AtomicNuclearProperties/index.html

[8] R. F. Hurley, V. A. Bashkirov, R. W. Schulte, A. J. Wroe, A. Ghebremedhin, P. Koss, B. Patyal, H. Sadrozinski, V. Rykalin, G. Coutrakon. Water-equivalent path length calibration of a prototype proton CT scanner. Med Phys. 2012 May;39(5):2438-46.